

CASE 3: RANS AND URANS APPLICATION WITH CFL3D

C. L. Rumsey

Computational Modeling & Simulation Branch, NASA Langley Research Center, Hampton, VA 23681-2199

Solution Methodology

This case was run using CFL3D, a multi-zone Reynolds-averaged Navier-Stokes code developed at NASA Langley [1]. It solves the thin-layer form of the Navier-Stokes equations in each of the (selected) coordinate directions. It can use 1-to-1, patched, or overset grids, and employs local time step scaling, grid sequencing, and multigrid to accelerate convergence to steady state. In time-accurate mode, CFL3D has the option to employ dual-time stepping with subiterations and multigrid, and it achieves second order temporal accuracy.

CFL3D is a finite volume method. It uses third-order upwind-biased spatial differencing on the convective and pressure terms, and second-order differencing on the viscous terms; it is globally second-order spatially accurate. The flux difference-splitting (FDS) method of Roe is employed to obtain fluxes at the cell faces. It is advanced in time with an implicit three-factor approximate factorization method.

Model Description

For this test case, three different turbulence models were used. The first is the one-equation Spalart-Allmaras model (SA) [2], the second is the two-equation shear-stress transport model of Menter (SST) [3, 4], and the third is an explicit algebraic stress model (EASM-ko) in $k-\omega$ form [5]. The first two models are both linear eddy-viscosity models that make use of the Boussinesq eddy-viscosity hypothesis, whereas the EASM-ko is a nonlinear model. The equations describing these three models can be found in their respective references.

In CFL3D, the models are implemented uncoupled from the mean-flow equations. They are solved using a three-factor implicit approximate factorization approach. The advection terms are discretized with first-order upwind differencing. The production source term is solved explicitly, while the advection, destruction, and diffusion terms are treated implicitly. For EASM-ko, the nonlinear terms are added to the Navier-Stokes equations explicitly.

Implementation and Case Specific Details

Three flow conditions are computed over the hump model: (1) no flow control, (2) steady suction flow control, and (3) oscillatory synthetic jet flow control. The control is applied near $x/c = 0.65$ on the back side of the hump, near where the flow separates in the un-controlled state. The freestream Mach number is $M = 0.1$, and the Reynolds number is approximately $Re = 936,000$ per hump chordlength. For the oscillatory case, the oscillation frequency is 138.5 Hz.

All computations performed for this case were 2-D. The grid used was the supplied 2-D structured grid number 1 (which contains 4-zones connected in a 1-to-1 fashion, and approximately 210,000 grid points), as well as a medium-level grid made from the fine grid by extracting every-other point in each coordinate direction (2-D structured grid number 2). The SA model was solved on both the fine and medium grids, whereas the SST and EASM-ko models were only solved on the medium grid. For the oscillatory case, only the SA model on the fine grid was used.

For the no-flow-control and steady suction cases, CFL3D was run in steady-state mode, utilizing local time-stepping to accelerate convergence. For the oscillatory case, the time step chosen yielded 360 time

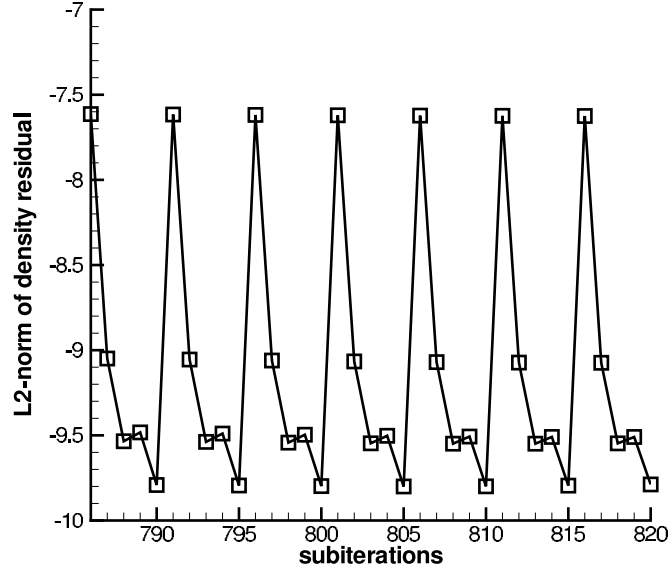


Figure 1: Convergence of subiteration residual during time-accurate oscillatory computation, SA model, fine grid.

steps per cycle of the forcing frequency, and 5 subiterations were employed per time step. For this case, this number of subiterations was enough to reduce the L_2 -norm of the subiteration density residual by about 2 orders of magnitude. See Fig. 1, which shows subiteration residual over the course of 7 time steps (with 5 subiterations per time step) during part of the unsteady cycle.

The boundary conditions were as follows. At the floor and hump surfaces, as well as at the side walls inside the cavity, solid wall adiabatic boundary conditions were applied. At the front of the grid, which extended to $x/c = -6.39$, far-field Riemann-type boundary conditions were applied. At the downstream boundary (at $x/c = 4.0$) the pressure was set at $p/p_{\text{ref}} = 0.99947$, and all other quantities were extrapolated from the interior of the domain. This back pressure was determined via trial and error, to achieve approximately the correct inflow conditions. At the bottom of the cavity, different boundary conditions were applied depending on the case. For the no-flow-control case, this wall was treated as an inviscid wall. For the steady suction case, the boundary condition set the velocity components as follows:

$$U = 0 \quad V = (\rho V)_{\text{set}} / \rho \quad (1)$$

and $(\rho V)_{\text{set}}$ was chosen in order to achieve the equivalent of a mass flow of 0.01518 kg/s through a 23-inch span. The value used turned out to be $(\rho V)_{\text{set}} = -0.001248 \rho_{\text{ref}} a_{\text{ref}}$, where a_{ref} is the reference speed of sound. For the oscillatory flow case, the boundary condition set the velocity components as follows:

$$U = 0 \quad V = [(\rho V)_{\text{max}} / \rho] \cos(2\pi F t) \quad (2)$$

where F is the frequency and t is the time, and $(\rho V)_{\text{max}}$ was chosen in order to achieve a maximum velocity magnitude near to the target of approximately 26.6 m/s out of the slot during the cycle. Fig. 2 shows the velocity magnitude at a position near the center of the slot exit as a function of nondimensional time, on a line even with the hump surface, over the course of one cycle of oscillation. The value of $(\rho V)_{\text{max}}$ used to achieve this condition was $(\rho V)_{\text{max}} = 0.001 \rho_{\text{ref}} a_{\text{ref}}$. Along with the above boundary conditions given by

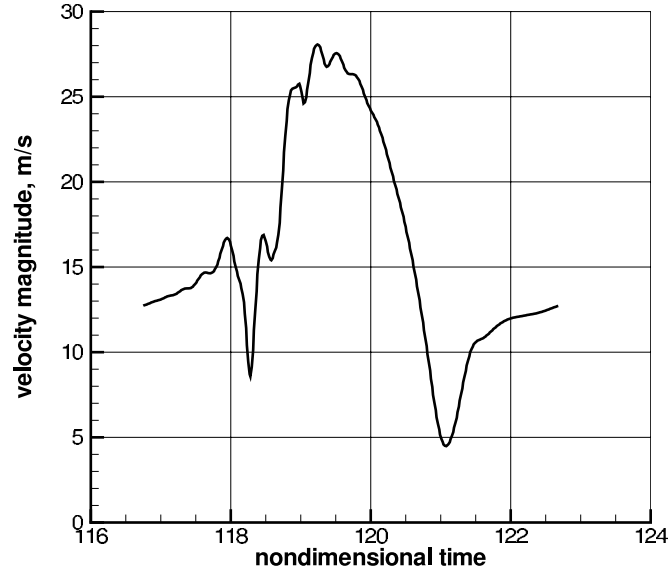


Figure 2: Velocity magnitude at the slot exit for oscillatory case, SA model, fine grid.

Eqs. 1 and 2, the density and pressure at the bottom of the cavity are extrapolated from the interior of the domain.

The top tunnel wall was treated as an inviscid wall for all of the computations submitted to the workshop. However, the effect of making the top wall a viscous wall was also investigated (using a different grid with appropriate finer normal spacing near the top wall). Resulting surface pressure coefficients are shown in Fig. 3. Using viscous top wall lowers the peak C_p levels over the center of the hump, in better agreement with experiment. However, the effect does not fully account for the difference between CFD and experiment. Also, the viscous upper wall does not impact the C_p levels in the separated region to any significant degree.

As a nonlinear model, EASM-ko can do a better job predicting the turbulent normal stresses than linear models. This can be seen in Fig. 4, which shows results predicted by the three models at $x/c = -2.14$. The linear models show no perceptible difference between $\overline{u'u'}$ and $\overline{v'v'}$, whereas EASM-ko does predict a normal stress difference. The $\overline{u'u'}$ from EASM-ko is in better agreement with the experiment, although its peak near the wall is still too low. There were no measurements of $\overline{v'v'}$.

Examples of the effects of grid and turbulence model can be seen in Fig. 5. This figure shows streamwise velocity profiles in the separated region at $x/c = 0.8$ for the suction case, using SA on both the fine and medium grids, and using SST and EASM-ko on the medium grid. There is essentially no difference between the SA results on the fine and medium grids, and the two-equation models both predict a qualitatively different profile than SA at this location.

References

- [1] Krist, S. L., Biedron, R. T., and Rumsey, C. L., "CFL3D User's Manual (Version 5.0)", NASA TM-1998-208444, June 1998.
- [2] Spalart, P. R., and Allmaras, S. R., "A One-Equation Turbulence Model for Aerodynamic Flows," *La Recherche Aeronautique*, No. 1, 1994, pp. 5–21.

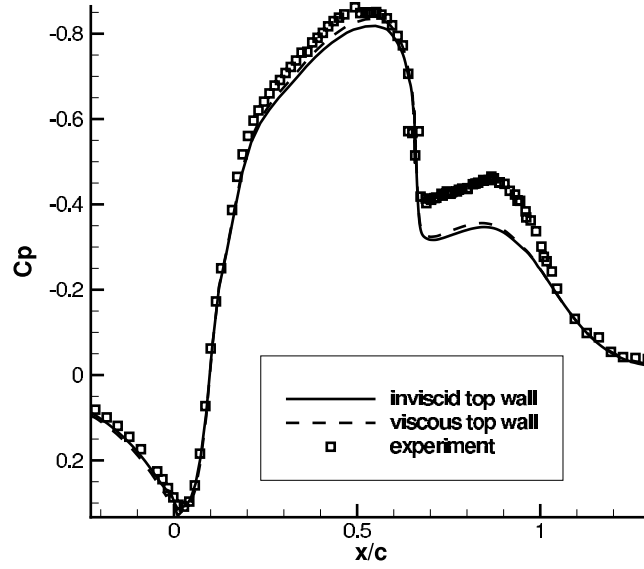


Figure 3: Surface pressure coefficients for no-flow-control case, SA model, medium grid.

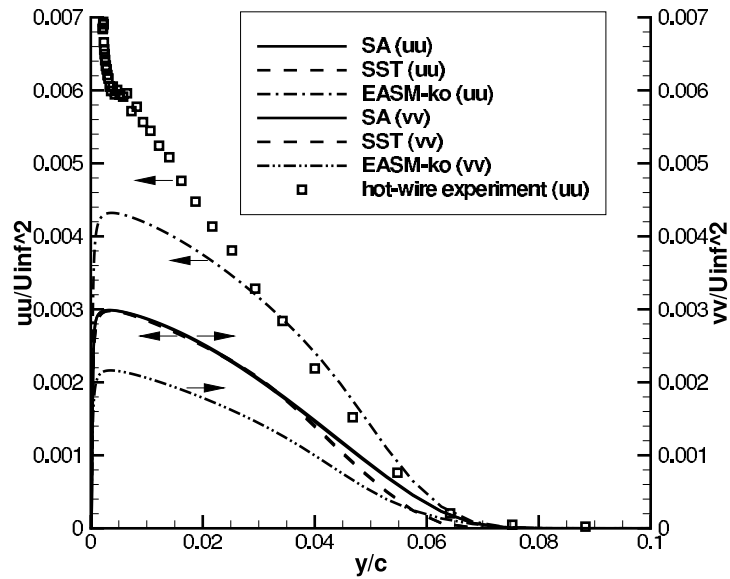


Figure 4: Predicted turbulent normal stresses at $x/c = -2.14$, medium grid.

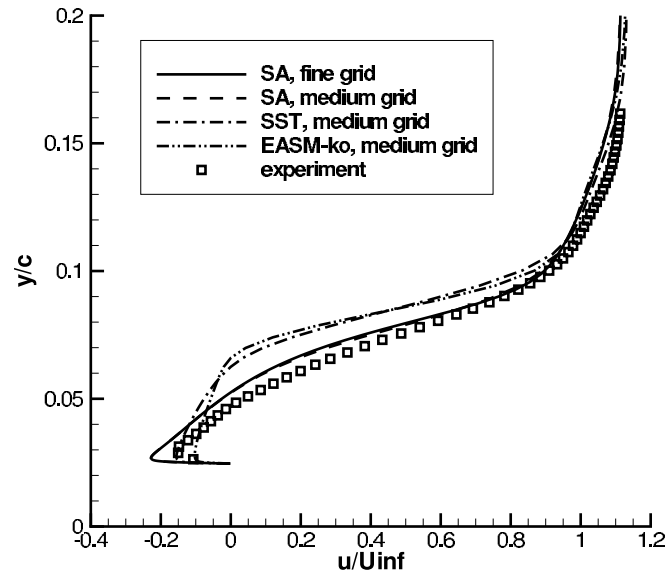


Figure 5: Velocity profiles at $x/c = 0.8$ for the suction case.

- [3] Menter, F. R., “Two-Equation Eddy-Viscosity Turbulence Models for Engineering Applications,” *AIAA Journal*, Vol. 32, No. 8, 1994, pp. 1598–1605.
- [4] Menter, F. R., Rumsey, C. L., “Assessment of Two-Equation Turbulence Models for Transonic Flows,” AIAA Paper 94-2343, Colorado Springs, CO, 1994.
- [5] Rumsey, C. L., Gatski, T. B., “Summary of EASM Turbulence Models in CFL3D With Validation Test Cases,” NASA/TM-2003-212431, June 2003.

CASE 3: TWO-DIMENSIONAL SIMULATION OF FLOW OVER A HUMP MODEL WITH MENTER'S SST MODEL

V. Katam, H. Chen, L. Huang, V. Parimi, R. P. LeBeau, and P. G. Huang

Department of Mechanical Engineering, University of Kentucky, Lexington, KY 40506-0108

Introduction

Flow control of separation is an ongoing topic of investigation. This investigation of the phenomenon is based on our CFD experience working on flow control approaches such as morphing wings[1] and blowing and suction jets [2,3]. The latter studies were performed with the CFD code GHOST. It is this code and its techniques that we have applied to solve the current flow control problem.

Solution Methodology

All present computations were performed with the CFD code, GHOST. GHOST is an in-house CFD code developed at University of Kentucky by P. G. Huang. The code is based on a finite volume structured formulation with chimera overset grids. The QUICK and TVD schemes are applied to discretize the convective terms in the momentum and turbulence equations, respectively; the central difference scheme is used for the diffusive terms and the second order upwind time discretization is employed for the temporal terms. This code has been tested extensively and is routinely used for turbulence model validation [4,5,6]. The turbulence model used in the present computation is Menter's SST two equation model [7], which provides excellent predictive capability for flows with separation [8]. The multi-block and chimera features of the code allow the use of fine grid patches near the jet entrance and in regions of highly active flow. The code also employs MPI parallelization to allow different computational zones to be solved on different processors. The computations were performed on multiple commodity PC clusters housed with our research group at the University of Kentucky.

Model Description

The turbulence model used is Menter's SST two equation model[7].

Implementation and case specific details

Grid #1 (Dense grid) and Grid #2 (Coarse grid) provided on the workshop website were used for the computation.

Specifying the boundary conditions proved to be a key question in this case. The upstream portion of the grid until $x/c = -2.14$ was removed so that the measured u velocity profile and streamwise turbulent intensity values were given as the inlet boundary condition. Several boundary conditions such as inviscid wall, freestream, and no-slip (viscous) wall were tested for the upper and the bottom boundary of the slot cavity. The best results were obtained for the boundary condition of a viscous wall on top and a viscous wall at the bottom of the suction cavity for the no flow case (Figure [1]). For steady suction cases, the boundaries remained the same except the bottom cavity boundary had a fixed velocity producing the workshop-provided mass flow rate.

A simulation with steady suction and a simulation with no suction were performed on each grid. In each case, a steady-state and a time-dependent simulation were calculated. The steady-state runs were done for a sufficient number of iterations until the flow data has converged to a constant solution. Turbulence statistics were obtained from the time-dependent simulation; all other data was taken from the steady-state results. Since the time-dependent simulations were performed only to obtain turbulence data, we used only a single timestep value for each case, corresponding to 0.001 seconds.

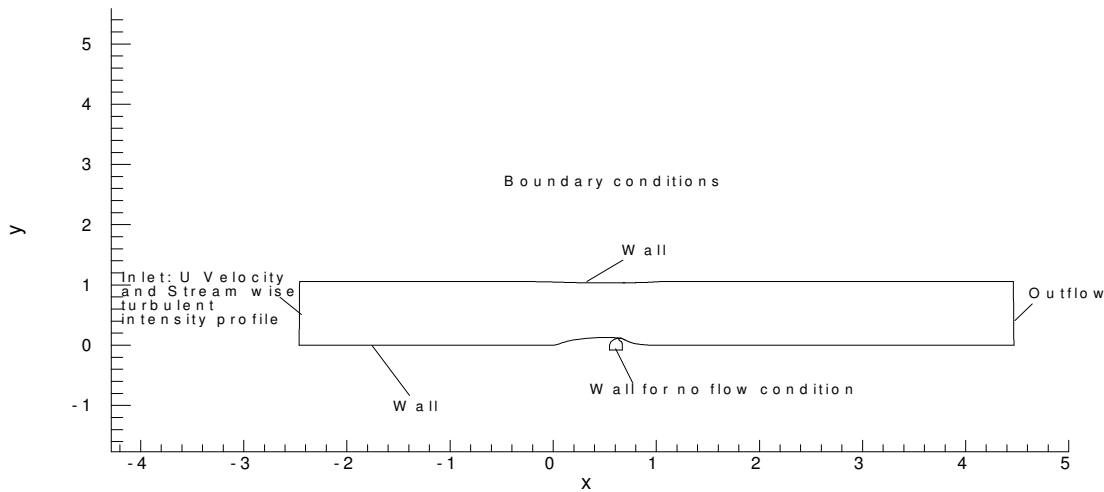


Figure 1: Boundary conditions used for the computation. All walls are viscous.

References:

1. Munday, D., Jacob, J.D., Hauser, T., and Huang, P.G., "Experimental and Numerical Investigation of Aerodynamic Flow Control Using Oscillating Adaptive Surfaces," AIAA 2001-2837, June. 2002.
2. L. Huang, P.G. Huang, R.P. LeBeau and Th. Hauser, "Numerical Study of Blowing and Suction Control Mechanism on NACA0012 Airfoil", *Journal of Aircraft*, (accepted for publication October, 2003).
3. L. Huang, G. Huang, R. LeBeau, Th. Hauser, "Optimization of Blowing and Suction Control on NACA0012 Airfoil Using Genetic Algorithm", AIAA 2004-0225 42nd Aerospace Sciences Meeting and Exhibit, Jan. 2004
4. Y. B. Suzen, P. G. Huang, "Numerical Simulation of Wake Passing on Turbine Cascades", AIAA-2003-1256, 41st Aerospace Sciences Meeting and Exhibit, Jan. 2003
5. Y. B. Suzen, P.G. Huang, R. J. Volino, T. C. Corke, F. O. Thomas, J. Huang, J. P. Lake and P. I. King, "A Comprehensive CFD Study of Transitional Flows In Low-Pressure Turbines Under a Wide Range of Operation Conditions", 33rd AIAA Fluid Dynamic Conference, AIAA 2003-3591, Jun. 2003
6. Y. B. Suzen and P. G. Huang, "Predictions of Separated and Transitional Boundary Layers Under Low-Pressure Turbine Airfoil Conditions Using an Intermittency Transport Equation", *Journal of Turbomachinery*, Vol. 125, No.3, Jul. 2003, pp. 455-464
7. F. R. Menter, "Two-Equation Eddy-Viscosity Turbulence Models For Engineering Applications", *AIAA Journal*, Vol. 32, No. 8, Aug. 1994, pp. 1598-1605

8. Bardina, J. E., P. G. Huang and T. J. Coakley, “Turbulence Modeling Validation, Testing and Development”, NASA TM-110446, Apr. 1997

CASE 3: Two-Dimensional Flow Control Analysis on the Hump Model

Sally A. Viken

Flow Physics and Control Branch, NASA Langley Research Center, Hampton, VA 23681-2199

Introduction

Computational analyses have been conducted on the Wall-mounted Glauert-Goldschmied type body (“hump” model) with the Full Unstructured Navier-Stokes 2-D (FUN2D) flow solver developed at NASA LaRC. This investigation uses the time-accurate Reynolds-averaged Navier-Stokes (RANS) approach to predict aerodynamic performance of the active flow control experimental database for the hump model. The workshop is designed to assess the current capabilities of different classes of turbulent flow solution methodologies, such as RANS, to predict flow fields induced by synthetic jets and separation control geometries. The hump model being studied is geometrically similar to that previously tested both experimentally and computationally at NASA LaRC [ref. 1 and 2, respectively].

Solution Methodology

The FUN2D flow solver is a node based, implicit, upwind flow solver used for computing flows around airfoil configurations discretized with an unstructured grid [ref. 3]. The governing equations (provided below) are the time-dependent RANS equations in conservation-law form, which are integrated in time to obtain a steady state solution. The inviscid fluxes are obtained on the faces of each control volume by using the flux-difference-splitting (FDS) technique of Roe [ref. 4]. A node-based algorithm is used in which the variables are stored at the vertices of the mesh and the equations are solved on non-overlapping control volumes surrounding each node. The viscous terms are evaluated with a finite-volume formulation that results in a central-difference-type scheme. The Spalart-Allmaras (SA) turbulence model is used in this investigation and all computations assume fully turbulent flow [ref. 5].

A two level iteration is used to achieve convergence of the discrete algebraic equations at each time-step. The outer iteration is a modified Newton method and employs a first-order Van Leer Jacobian (LHS) [ref. 6] driving the second-order residual vector (RHS). The inner iteration employs a red-black Gauss Seidel point-implicit algorithm to solve the equations at each step of the outer iteration. Twenty inner sub-iterations were used in all cases in this study. The SA turbulence model equations are weakly coupled to the hydrodynamic equation via the outer loop iteration.

For steady state computations, the solution is driven to convergence using an Euler implicit advancement in pseudo-time. For time-dependent computations, the solution is discretized in physical time with the second-order backwards differentiation formulae (BDF), while pseudo-time iterations are again employed to relax the equations [ref. 2, 7]. The linear system of equations resulting from either formulation is iteratively solved with a point-implicit procedure.

Governing Equations

The governing equations, the Reynolds-averaged Navier-Stokes equations, are written in conservative-law form to relate the rate of change of mass, momentum, and energy in a control volume of area A to the fluxes of these quantities through surface of the control volume. The non-dimensional equations presented in vector form are as follows:

$$A \cdot \frac{\partial \mathcal{Q}}{\partial t} + \oint_{\partial \Omega} \vec{F}_i \cdot \hat{n} \, dl - \oint_{\partial \Omega} \vec{F}_v \cdot \hat{n} \, dl = 0$$

where $\hat{\mathbf{n}}$ is the outward-pointing unit normal to the surface of the control volume $\partial\Omega$. The solution vector \mathbf{Q} containing the dependent variables is defined by

$$\mathbf{Q} = \begin{Bmatrix} \rho \\ \rho u \\ \rho v \\ E \end{Bmatrix}$$

The inviscid and viscous flux vectors through the surface of the control volume $\partial\Omega$, defined as $\vec{\mathbf{F}}_i$ and $\vec{\mathbf{F}}_v$, respectively, are given by

$$\vec{\mathbf{F}}_i = \mathbf{f}\hat{i} + \mathbf{g}\hat{j} = \begin{Bmatrix} \rho u \\ \rho u^2 + p \\ \rho uv \\ (E + p)u \end{Bmatrix} \hat{i} + \begin{Bmatrix} \rho v \\ \rho vu \\ \rho v^2 + p \\ (E + p)v \end{Bmatrix} \hat{j}$$

$$\vec{\mathbf{F}}_v = \mathbf{f}_v\hat{i} + \mathbf{g}_v\hat{j} = \begin{Bmatrix} 0 \\ \tau_{xx} \\ \tau_{xy} \\ u\tau_{xx} + v\tau_{xy} - q_x \end{Bmatrix} \hat{i} + \begin{Bmatrix} 0 \\ \tau_{yx} \\ \tau_{yy} \\ u\tau_{yx} + v\tau_{yy} - q_y \end{Bmatrix} \hat{j}$$

The normal and shear stress terms and heat conduction terms are defined by

$$\tau_{xx} = (\mu + \mu_t) \frac{M_\infty}{\text{Re}} \frac{2}{3} [2u_x - v_y]$$

$$\tau_{yy} = (\mu + \mu_t) \frac{M_\infty}{\text{Re}} \frac{2}{3} [2v_y - u_x]$$

$$\tau_{xy} = (\mu + \mu_t) \frac{M_\infty}{\text{Re}} [u_y + v_x]$$

$$q_x = \frac{-M_\infty}{\text{Re}(\gamma-1)} \left(\frac{\mu}{\text{Pr}} + \frac{\mu_t}{\text{Pr}_t} \right) \frac{\partial a^2}{\partial x}$$

$$q_y = \frac{-M_\infty}{\text{Re}(\gamma-1)} \left(\frac{\mu}{\text{Pr}} + \frac{\mu_t}{\text{Pr}_t} \right) \frac{\partial a^2}{\partial y}$$

The equation of state for a perfect gas is used to define the pressure p

$$p = (\gamma - 1) \left\{ E - \rho \frac{(u^2 + v^2)}{2} \right\}$$

and the laminar viscosity μ is determined through Sutherland's law

$$\frac{\mu}{\mu_\infty} = \frac{(1 + C^*) \left(\frac{T}{T_\infty} \right)^{\frac{3}{2}}}{\left(\frac{T}{T_\infty} + C^* \right)}$$

where $C^* = \frac{198.6}{536.4}$ is Sutherland's constant divided by a free stream reference temperature which is defined to be 536.4° Rankine for Case Study #3.

The eddy viscosity, μ_t , is obtained by the turbulence closure model developed by Spalart and Allmaras [ref 5]. Again, the turbulent viscosity equation is solved separately from the flow equations at each time step, using the Euler implicit time-stepping scheme, resulting in a loosely coupled solution process.

Implementation and Case Specific Details

Unstructured Grids

Two-dimensional unstructured grids were generated for Case Study #3 analyses and provided at the website. The coordinates used for the unstructured grids were the 2-D non-dimensionalized theoretical model coordinates along with the tunnel geometry. These grids were generated with advancing front type point placement with iterative local re-meshing for grid quality improvement [ref. 8,9]. For the internal flow analyses conducted with the FUN2D code that will be presented at the workshop, the website unstructured Grid #1 and #2 were used. The forward extent of these grids is longer than the actual splitter plate length used in the wind tunnel experiment. These grids ran from -6.39c ahead of the leading edge of the model to 4.0c behind the leading edge of the model. This grid extent of -6.39c was chosen because it was found in preliminary CFD tests to yield a "run" long enough so that the computed boundary layer thickness *approximately* matched that of experimental data at $x/c = -2.14$ [figure 1]. The grid height is $y/c = 0.90905$, which corresponds with the actual height of 15.032 inches from the splitter plate to the ceiling of the tunnel test section. In addition, these grids were generated with the internal cavity modeled. The fine grid (website unstructured Grid #1) has 123703 nodes, 368476 faces, and 247404 cells. The minimum spacing at the viscous walls was set to be approximately 8.e-06. This minimum spacing yields a y^+ value less than 1. The coarse grid (website unstructured Grid #2) has 57152 nodes, 169689 faces, and 114302 cells. The minimum spacing at the viscous walls was set to be approximately 1.6e-05. The upper grid boundary (test section ceiling) was set up to use inviscid-type grid spacing.

Initial calculations were conducted on the hump model using the grids described above for the baseline no-flow control condition. The experimental data for the baseline case showed a discontinuity in the C_p distribution at $x/c = 0.48$, which was not observed in the computational results. An unstructured grid was generated using the Quality Assurance (QA) coordinates provided at the website followed by further computational analyses. This grid has 122790 nodes, 365737 faces, and 245578 cells, with the minimum wall spacing yielding a y^+ value less than 1. Computational results for the baseline no-flow condition analyzed with the QA coordinate grid and theoretical coordinate grid are compared with the experimental data [figure 2]. Computations with the QA grid show the sensitivity of the solution to the discontinuity in the hump model

surface geometry similar to that found experimentally. Outside of this localized discontinuity in the C_p distribution, the CFD solutions obtained with the QA coordinate grid and the theoretical coordinate grid compared well together. Grid studies were also conducted with the upper grid boundary defined to have viscous wall spacing, however only a slight increase in the flow acceleration over the hump model was achieved. All computations that will be presented at the workshop were run using the grids generated with the theoretical coordinates (unstructured Grids #1 and #2) that have inviscid-type grid spacing on the upper grid boundary.

Boundary Conditions

The boundary conditions on the hump model, the internal cavity walls, and the tunnel floor corresponded to no-slip between the fluid and the solid boundary at their interface, with a constant temperature wall that was set to the adiabatic wall temperature T_{aw} . The tunnel ceiling was treated as an inviscid surface. The internal "actuator" boundary at the bottom of the hump cavity was also treated as an inviscid surface for the baseline cases with no control. For the control cases, the "actuator" boundary condition corresponded to $\rho V(\xi, \eta = 0, t) = \text{Amplitude} * f(\xi) * \cos(\omega t)$ where $f(\xi) = 1$ (tophat distribution). The mass flux through the "actuator" boundary of the internal cavity was adjusted to obtain a peak velocity near 26.6 m/sec at the slot exit during the blowing part of the cycle [$(\rho V)_{\max} = 0.001(\rho_{\text{ref}} a_{\text{ref}})$ was used to obtain this condition]. For inflow conditions, temperature was also specified on the "actuator" boundary from the experimental data. To obtain the boundary conditions at the tunnel inlet, the flow was assumed to be both inviscid and isentropic in this region so that quantities for the computation of the flux along the inflow boundary were obtained from two locally 1-D Riemann invariants. The Riemann invariants were considered constant along characteristics defined normal to the inflow boundary. At the downstream boundary, a back pressure of 0.99947 times reference pressure was specified in order to approximate the upstream conditions at the tunnel inlet.

Time-Step

The baseline and steady suction cases were run non-time-accurate, and achieved steady state convergence. The oscillatory suction/blowing case was run time-accurately using the second-order accurate Backward Differentiation Formulae (BDF) scheme. The assumption was made that the excitation frequency introduced at the "actuator" boundary was a perfect sine wave. The computational oscillatory cases were run time-accurately at least 20 shedding cycles to set up the flow field and then the C_p 's were averaged over 20 cycles.

Test Conditions

Computational flow analyses were conducted on the hump model for $M_\infty = 0.1$, at $Re = 936000$. The two required test conditions for Case Study #3 were conducted along with the optional condition; the no-flow through the span slot, the suction case with suction rate of 0.01518 kg/sec through the slot, and the zero-net-mass-flux oscillatory suction/blowing case (frequency = 138.5 Hz, and peak velocity out of slot during blowing part of cycle = 26.6 m/s). Only two-dimensional computations were performed for these studies.

An example of the grid density effects are shown in figure 3, where the streamwise velocity profiles in the separated flow region at $x/c = 0.8$ for the suction case can be observed. The profiles for the fine and coarse level grids show that the grids are sufficiently resolved for the case analyzed.

REFERENCES

1. Seifert, A., and Pack, L. G., "Active Flow Separation Control on Wall-Mounted Hump at High Reynolds Numbers." AIAA Journal, Vol. 40, No. 7, July 2002.
2. Viken, S., Vatsa, V., and Rumsey, C., "Flow Control Analysis of the Hump Model with RANS Tools". AIAA 2003-0218, January 2003.

3. Anderson, W. K., and Bonhaus, D. L., "An Implicit Upwind Algorithm for Computing Turbulent Flows on Unstructured Grids," *Computers & Fluids*, Vol. 23, No. 1, 1994, pp. 1-21.
4. Roe, P., "Approximate Riemann Solvers, Parameter Vectors, and Difference Schemes," *J. of Comp. Phys.*, Vol. 43, 1981, pp. 357-372.
5. Spalart, P.R. and Allmaras, S.R., "A One- Equation Turbulence Model for Aerodynamic Flows," AIAA 92-0439, January, 1992.
6. Van Leer, B., "Flux Vector Splitting for the Euler Equations," *Lecture Notes in Physics*, Vol. 170, 1982, pp. 501-502.
7. Carpenter, M. H., Viken, S. A., Nielsen, Eric J., "The Efficiency of High Order Temporal Schemes," AIAA Paper 2003-6334, January 2003.
8. Marcum, D. L., "Generation of Unstructured Grids for Viscous Flow Applications," AIAA Paper 95-0212, January 1995.
9. Marcum, D. L., and Weatherhill, N. P., "Unstructured Grid Generation Using Iterative Point Insertion and Local Reconnection," *AIAA Journal*, Vol. 33, No. 9, September 1995.

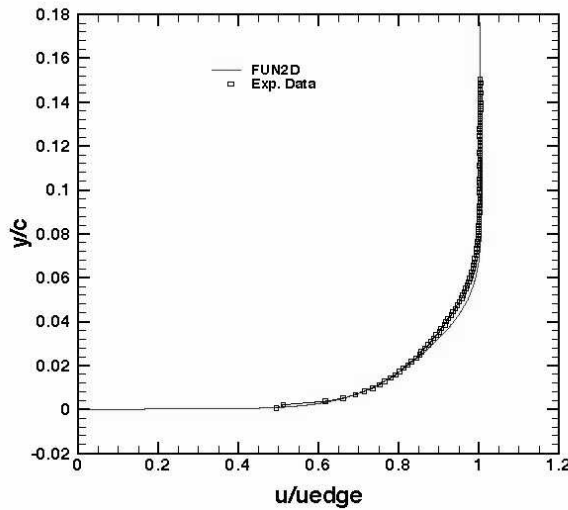


Figure 1. Velocity profile at $x/c = -2.14$ for baseline case ($M_\infty = 0.1$; $Re = 936000$).

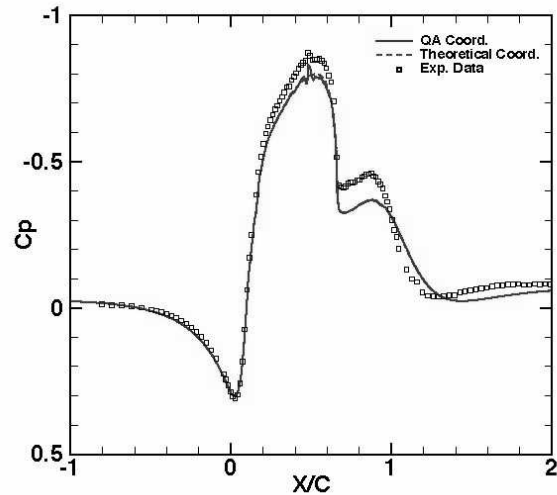


Figure 2. Baseline computational results versus experimental data ($M_\infty = 0.1$; $Re = 936000$).

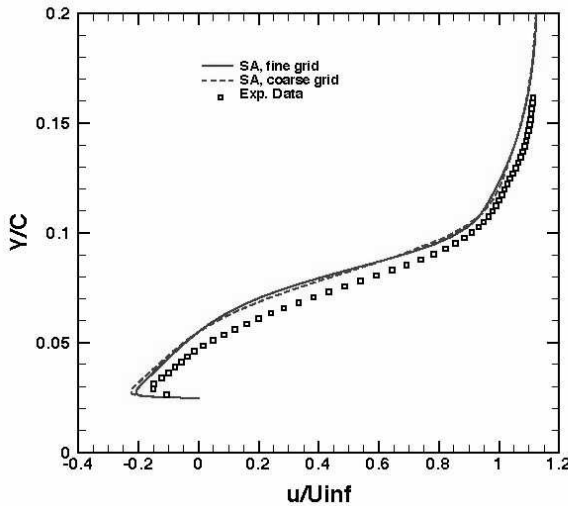


Figure 3. Velocity profiles at $x/c = 0.8$ for the suction case ($M_\infty = 0.1$; $Re = 936000$).

Case 3: Separated Flows—An Assessment of the Predictive Capability of Five Common Turbulence Models

R.E. Spall, W.F. Phillips, and N.R. Alley
Department of Mechanical and Aerospace Engineering
Utah State University, Logan, UT 84322-4130

Introduction

The results presented herein were generated using the commercial CFD solver Fluent, which makes available to the user a relatively large number of turbulence model options. Fluent is widely used in both industry and academia, and it was of interest to the authors to assess the applicability of the available models in predicting separated flows. Our interest is also derived, in part, from our use of the code in the design of high lift, unmanned aerial vehicles (UAV's) in which the ability to predict flow separation is crucial.

Solution Methodology

The results were computed using the commercial CFD solver Fluent (version 6.18). Fluent employs a pressure-based finite volume solution procedure to solve the governing equations on unstructured grids. Pressure-velocity coupling was accomplished using the SIMPLEC procedure. Second-order central differencing was used for the viscous terms in the transport equations. Interpolation to cell faces for the convection terms was performed using a third-order QUICK scheme. In all cases, a steady, two-dimensional formulation was employed. Solutions obtained using a segregated solver were considered converged when residuals for each of the equations (based on an L2 norm) were reduced by a minimum of five orders of magnitude. Additional iterations were then performed to confirm iterative convergence.

Model Description

Five different turbulence models available in the commercial CFD solver Fluent were used to solve test case 3. These models included 1) $k - \epsilon$, 2) $k - \omega$, 3) Reynolds stress transport, 4) Spalart-Almaras, and 5) shear stress transport (SST). In all cases, the near wall mesh within the channel region along the lower wall was sufficiently fine so that wall functions were never implemented. A brief description of each model appears below, with an emphasis on describing methodology that often varies within each class of model.

1) The $k - \epsilon$ model

The standard $k - \epsilon$ model of Launder and Spalding [1] was employed, with low-Reynolds number modifications for the near-wall modeling, which combine a two-layer model with wall functions. In the present work, the near wall mesh was fine enough to resolve the viscous sublayer; consequently the two-layer model was used and wall functions were never implemented. In particular, if $Re_y < Re_y^*$ (where $Re_y^* = 200$) the one-equation model of Wolfstein [2] is employed.

In this region, the equation for k is retained, but the turbulent viscosity is obtained from $\mu_{t,i} = \rho C_\mu l_\mu \sqrt{k}$ where the length scale is given as $l_\mu = y c_l (1 - e^{-Re_y/A_\mu})$ [3]. The turbulent viscosity determined above is then smoothly blended with the high Reynolds number $\mu_{t,o}$ obtained in the outer region. The dissipation rate in the near wall region is also specified algebraically as $\varepsilon = k^{3/2}/l_\varepsilon$ where the length scale, l_ε , is computed using the same relation used in the specification of the turbulent viscosity, although with a different value of the constant A . A blending function is used to ensure a smooth transition between ε specified algebraically in the inner region, and ε computed via the transport equation in the outer region. The blending is of the form $\mu_t = \lambda \mu_{t,o} + (1 - \lambda) \mu_{t,i}$ (1) where,

$$\lambda = \frac{1}{2} \left[1 + \tanh \frac{(Re_y - Re_y^*)}{A} \right] \quad (2)$$

2) The $k - \omega$ model

A low-Reynolds number version of the Wilcox $k - \omega$ model [4] was employed. In particular, a low Reynolds number correction to the turbulent viscosity, $\mu_t = \alpha^* \rho k / \omega$, is determined as:

$$\alpha^* = \alpha_\infty^* \left(\frac{\alpha_0^* + Re_t / Re_k}{1 + Re_t / Re_k} \right), \quad (3)$$

where $Re_t = (\rho k) / (\mu \omega)$, $Re_k = 6$, $\alpha_0^* = \beta_i / 3$, $\alpha_\infty^* = 1$, and $\beta_i = 0.072$. A low-Reynolds number correction is also applied to the production of ω term, $G_\omega = \alpha \omega G_k / k$, as:

$$\alpha = \frac{\alpha_\infty}{\alpha^*} \left(\frac{\alpha_0 + Re_t / R_\omega}{1 + Re_t / R_\omega} \right) \quad (4)$$

where $\alpha_\infty = 0.52$ and $R_\omega = 2.95$. In terms of boundary conditions, the asymptotic value of ω at the wall is specified as:

$$\omega_w = \rho (u^*)^2 \omega^+ / \mu. \quad (5)$$

The value of ω^+ is determined from:

$$\omega^+ = \min \left[2500, \frac{6}{\beta_\infty^* (y^+)^2} \right], \quad (6)$$

where $\beta_\infty^* = 0.09$.

3) Reynolds stress transport model

The RST model also uses a two-layer formulation for the near wall, similar to that used for the $k - \varepsilon$ model. In this case, modifications to the linear pressure-strain model follow the methodol-

ogy given in Launder and Shima [5]. These modifications involve specification of the constants multiplying the slow and rapid pressure strain terms, and the wall-reflection term, in terms of Reynolds stress invariants and the turbulent Reynolds number. Diffusive transport is modeled using a scalar turbulent diffusivity [6], given as:

$$D_{T,ij} = \frac{\partial}{\partial x_k} \left(\frac{\mu_t}{\sigma_k} \frac{\partial \overline{u_i' u_j'}}{\partial x_k} \right). \quad (7)$$

4) Spalart-Allmaras

The Spalart-Allmaras model [7] solves a transport equation for a variable that is a modified form of the turbulent kinematic viscosity. For the results presented, the deformation tensor, S , appearing in the production term follows the original model proposed by Spalart and Allmaras, which is based on the magnitude of the vorticity $S = \sqrt{2\Omega_{ij}\Omega_{ij}}$, where Ω_{ij} is the mean rate-of-rotation tensor. Fluent also incorporates a modified definition of S which includes measures of both rotation and strain tensors in its definition; however, this modification was not used.

5) Shear Stress Transport

Fluent provides a low-Reynolds number version of the SST model, which was employed for the results presented. In particular, the turbulent viscosity was determined as:

$$\mu_t = \frac{\rho k}{\omega} \frac{1}{\max \left[\frac{1}{\alpha^*}, \frac{\Omega F_2}{\alpha_1 \omega} \right]} \quad (8)$$

where α^* is as defined for the $k - \omega$ model and $\Omega = \sqrt{2\Omega_{ij}\Omega_{ij}}$. In addition, the turbulent Prandtl numbers are defined as:

$$\sigma_k = \frac{1}{F_1/\sigma_{k,1} + (1 - F_1)/\sigma_{k,2}} \quad (9)$$

$$\sigma_\omega = \frac{1}{F_1/\sigma_{\omega,1} + (1 - F_1)/\sigma_{\omega,2}} \quad (10)$$

where F_1 and F_2 are blending functions. In addition, $\sigma_{k,1}$ and $\sigma_{k,2}$ are constant inner and outer turbulent Prandtl numbers, respectively. (Similarly for $\sigma_{\omega,1}$ and $\sigma_{\omega,2}$.)

Implementation

The inlet u -velocity boundary condition was specified using the experimental profile available on the web site. The v -velocity was set to zero. Turbulence quantities were derived from the approximate inlet turbulence intensity (I) of 0.09% (given on web site) and a turbulence length scale (l) which was defined as $0.4\delta_{0.99}$ (where $\delta_{0.99}$ is the boundary layer thickness at the inlet). In particular, the inlet turbulence kinetic energy was then set to $k = 1.5(\bar{u}I)^2$ where \bar{u} is the mean flow velocity. The dissipation rate was computed as $\epsilon = C_\mu^{0.75} k^{1.5}/l$. For the Spalart-Allmaras model,

the inlet modified viscosity was specified as $\tilde{\nu} = \sqrt{\frac{3}{2}} \bar{u} l$. When implementing the $k - \omega$ model, the inlet specific dissipation rate was computed from $\omega = k^{1/2} / (C_\mu^{1/4} l)$. Finally, for the RST model the inlet Reynolds stresses were specified as $\overline{u_i' u_j'} = 0$ and $\overline{u_k' u_k'} = (2/3)k$, where k was computed as described above. In all cases, zero normal derivative boundary conditions were used at the outflow plane. No-slip conditions were implemented on both the upper and lower walls. The model-specific approaches to implementing wall boundary conditions were described in the section on Model Description. (Slip wall conditions were also used on the upper wall, with little change in the resulting solutions. However, the results presented are for the no-slip conditions.)

Solutions were computed on two different grids, neither of which were those provided on the web site. The coarser grid consisted of 38,720 quadrilateral cells within the channel; the finer grid consisted of 85,760 cells. Grid points were clustered toward the wall so that in all cases $y^+ < 0.5$ for the lower wall adjacent cells. This was achieved by specifying the distance of the first grid point above the lower wall as $y = 0.000018c$. The grid spacing along the upper wall was defined such that $y^+ \approx 50$, so that wall functions were used. For the suction case, the suction chamber was included in the model and contained 2,169 tetrahedral cells. No grid refinement was performed within the suction chamber. The grids (either fine or coarse) within the channel section were identical for both the no-suction and suction cases. A section of the finer grid in the region of the suction slot is shown in Fig. 1.

References

1. Launder, B.E. and Spalding, D.B. *Lectures in Mathematical Models of Turbulence*. Academic Press, London, England, 1972.
2. Wolfstein, M. "The Velocity and Temperature Distribution of One-Dimensional Flow with Turbulence Augmentation and Pressure Gradient," *Int. J. Heat Mass Transfer*, Vol. 12, pp. 301-318, 1969.
3. Chen, H.C. and Patel, V.C. "Near-Wall Turbulence Models for Complex Flows Including Separation," *AIAA Journal*, Vol. 26, pp. 641-648, 1988.
4. Wilcox, D.C. *Turbulence Modeling for CFD*, DCW Industries, Inc., La Canada, California, 1998.
5. Launder, B.E. and Shima, N. "Second-Moment Closure for the Near-Wall Sublayer: Development and Application," *AIAA Journal*, Vol. 27, pp. 1319-1325, 1989.
6. Lien, F.S. and Leschziner, M.A. "Assessment of Turbulent Transport Models Including Non-Linear RNG Eddy-Viscosity Formulation and Second-Moment Closure," *Computers and Fluids*, Vol. 23, pp. 983-1004, 1994.
7. Spalart, P. and Allmaras, S. "A One-Equation Turbulence Model for Aerodynamic Flows," Technical Report AIAA-92-0439, American Institute of Aeronautics and Astronautics, 1992.

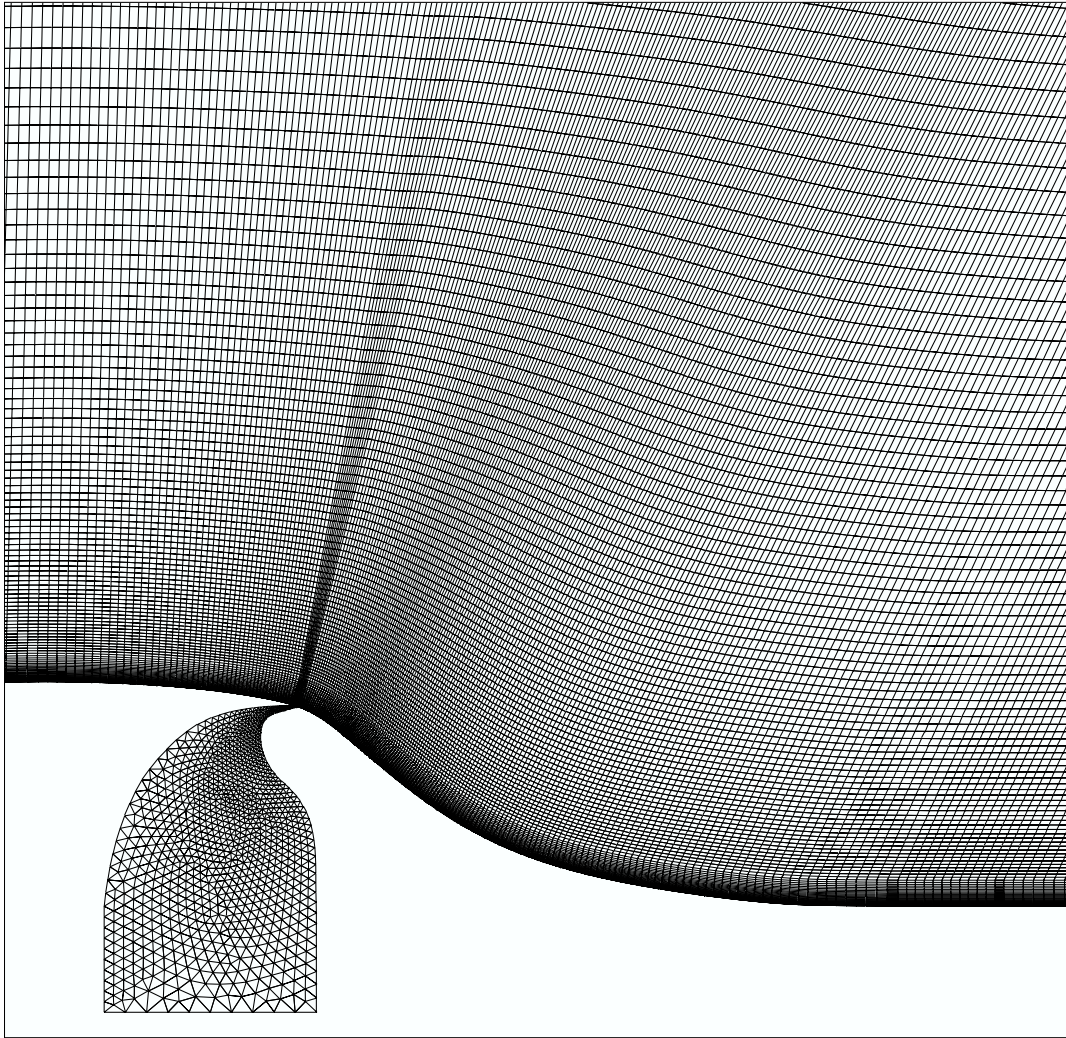


Figure 1. Mesh for Case 3 with flow control in the region of the suction slot. The grid consists of 85,760 quadrilateral cells in the channel region, and 2,169 tetrahedral cells in the suction chamber.

CASE 3: Active Control for Separated Flows

A. Shmilovich, Y. Yadlin, and R.W. Clark

Aerodynamic Technology, Flight Sciences/Advanced Design, Phantom Works, The Boeing Co., Huntington Beach, CA 92647

Introduction

A numerical procedure has been developed for the analysis of unsteady flows within the framework of active control. Computations have been performed for flows past airfoils, wings and engines, ranging from nearly static ambient conditions and up to transonic freestream velocities. The analysis tool has been extensively used to develop new and practical flow control approaches. Some of these applications include vortex control (by reducing core strength or by introduction of perturbations to destabilize the vortex) and separation control to enhance high lift performance over a wide range of flow conditions.

Solution Methodology

The numerical tool is a modified OVERFLOW code originally developed by NASA [1]. Overflow uses the Reynolds Averaged Navier Stokes formulation in conjunction with field turbulence models. A special module has been used for applying the time-varying boundary conditions. Various signal shapes can be used in conjunction with arbitrary stagnation properties for the general description of the jet.

Implementation and Case Specific Details

Several aspects of computations are described bellow.

Grid: The point-match grid provided by the workshop organizers has been used for these simulations with a slight modification. A narrow region of grid overlap has been introduced by extending the grid of the actuator into the wind-tunnel channel grid.

Turbulence models: SA and SST models have been used. Results in terms of pressure distributions and off surface streamwise velocity were very similar.

Boundary conditions: The program uses the mass flow rate, area and the stagnation pressure and temperature to define the velocity across the boundary. The orientation of the flux vector can also be prescribed and jet pulsation is obtained from the forcing frequency. General signal shapes ranging from sinusoidal to step-function are defined by a set of analytical functions. A sine wave representation of the jet is being employed in the oscillatory case.

Time steps: The time-accurate calculation for the pulsed jet case uses 800 steps per cycle. The calculation starts with a steady-state solution obtained for the flow in the absence of any excitation. Asymptotic quasi-state is achieved after approximately 20 cycles based on the normal force on the bump.

With respect to the pulsating actuation case it is instructive do discuss the issue of flow separation and reattachment. Fig. 1 shows the off-surface streamwise component of the velocity along the bump. The

instantaneous distributions at equal time intervals over one activation period (0.00722 seconds) show the transitory nature of the separation bubble. The onset of flow separation is directly affected by the intermittent ejection and suction at the orifice and the entrainment of the surrounding fluid. The size of the separation region and the movement of the reattachment point are being influenced by the oncoming flow and the impact occurs on a larger scale.

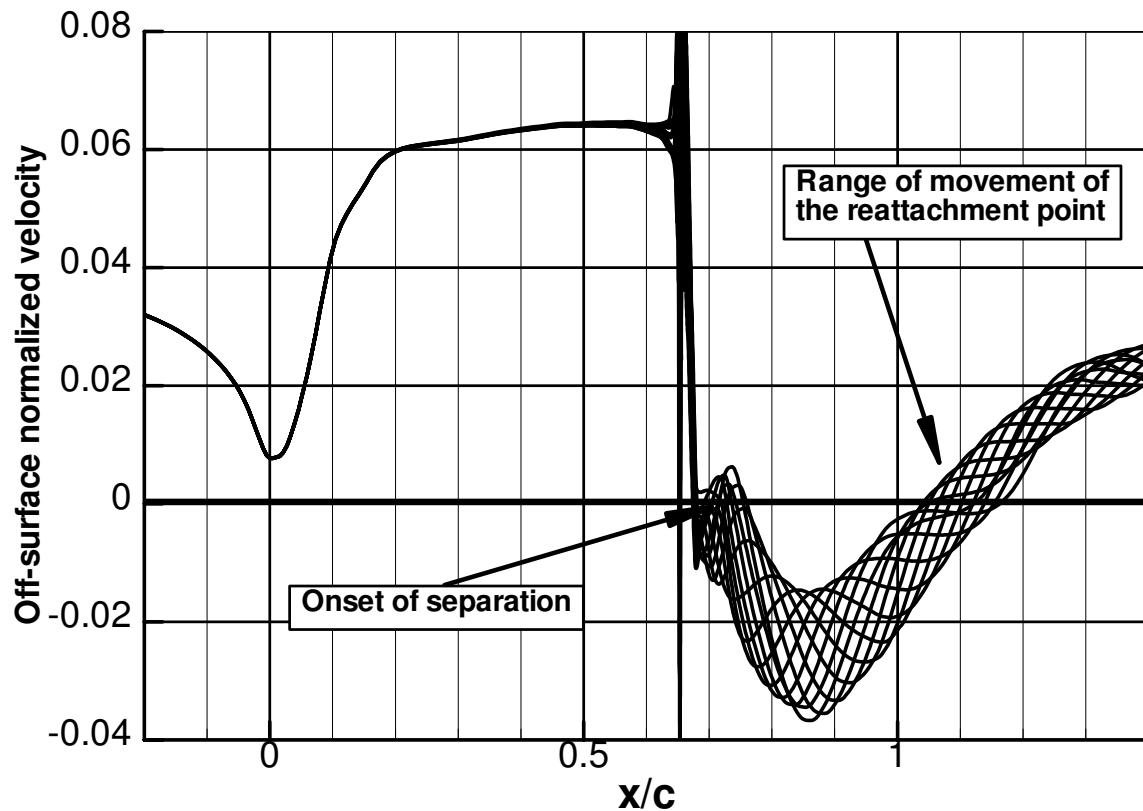


Figure 1: Extent of flow separation on the bump based on instantaneous off-surface streamwise component of the velocity (pulsed excitation case)

References

- [1] Buning, P.G. et al, "OVERFLOW User's Manual, Version 1.8j," NASA Langley Research Center, Hampton VA, 1999.

CASE 3: Investigation of a boundary condition model for the simulation of controlled flows

C. Marongiu¹, G.Iaccarino², P. Catalano¹, M. Amato¹

¹CIRA Italian Center for Aerospace Research Via Maiorise, Capua (CE) 81043 - Italy

²CTR Center for Turbulence Research Stanford University, Stanford CA 94305 - USA

Introduction

The aim of this work is to investigate the use of a boundary condition for the simulation of flows controlled by steady-unsteady mass injection/suction devices. These actuators usually consist of a deforming membrane oscillating inside a cavity. The simulation of the whole cavity would require a very complicated and time-consuming moving-mesh calculation. Therefore the use of a boundary condition applied at the cavity exit, the interface between the external and the internal domain, is an attractive strategy. This work is a first step towards investigating the limits and the benefits of the approach.

Results obtained by two unsteady RANS codes, the CIRA U-ZEN code, and FLUENT, a commercial CFD code, are reported for the flow around a two-dimensional bump. Several turbulence models are employed including one-, two- and four-equation models. The flow control is obtained via suction and it has been computed using two boundary conditions, corresponding to a top-hat distribution on the wall and to an inclined jet. The results have been compared with the experimental data and numerical computations including the whole cavity.

Computational Codes

U-ZEN

The CIRA U-Zen code solves the compressible RANS equations around complex aeronautical configurations using multiblock structured grids. The numerical discretization is based on a second order- cell centered finite volume method with explicit (fourth order) artificial dissipation. The unsteady procedure is based on the dual time stepping method where a pseudo steady-state problem is solved at each time step. Conventional convergence accelerators, including geometrical multigrid and residual smoothing, in the dual integration are used. Several turbulence models are available in U-ZEN [1]: for the numerical simulations presented in this work the Myong and Kasagi $k-\omega$ [2], and the SST Menter $k-\omega$ [3] turbulence model are used.

FLUENT

FLUENT is a commercial CFD code that solves the RANS equations on hybrid unstructured grids. It uses a second-order upwind discretization based on the SIMPLE pressure-velocity coupling and the formulation can accommodate compressible flows. Dual time stepping is used to obtain time accurate simulations and an algebraic multigrid technique is used to accelerate convergence within each time step. A multitude of turbulence models and variants are available in Fluent. In this work the Spalart Allmaras, SA, [4] model and Durbin's ν^2 - f four-equation model [5] are used. The ν^2 - f model was implemented in FLUENT using the User Subroutines [6].

Flow Simulations

Basemodel

The basemodel case has been studied as a two-dimensional flow. Several computational grids and turbulence models have been used. The aim is the evaluation of the accuracy of the predictions in terms of grid and inflow and outflow conditions. The domain extends for 2.14c upstream and 4c

downstream the hump. The height is 0.91c. The external boundary conditions are specified as follows:

$$\begin{array}{ll} \text{inflow} & \begin{array}{l} u \mid \text{from experimental data} \\ v \mid 0 \end{array} \end{array} \quad (1)$$

$$\frac{p}{p_{\infty}} \mid 1.2 \frac{1}{2} \frac{\psi_{\infty}}{p_{\infty}} \frac{\nu}{\nu_{\infty}} \frac{41}{\nu} \left| \frac{U_{\infty}^2}{4 U^2} \right|$$

$$\begin{array}{ll} \text{outflow} & \begin{array}{l} u \text{ and } v, \text{ extrapolated} \\ \frac{p}{p_{\infty}} \mid 0.99944 \end{array} \end{array} \quad (2)$$

$$\begin{array}{ll} \text{upper wall} & \text{slip wall} \end{array} \quad (3)$$

$$\begin{array}{ll} \text{lower wall} & \text{no slip wall} \end{array} \quad (4)$$

U-ZEN computations are carried out using the available grid on the CFDVAL2004 web site, (by C.Rumsey, GRID1) and the $k-\omega$ and the $k-\kappa$ turbulence models. The computation with the $k-\omega$ model has been repeated with a second grid (again available on CFDVAL2004 web site, supplied by C. Marongiu, GRID2). These three tests on the base model configuration have been performed with a turbulence level intensity equal to 0.09%. A fourth test has been performed imposing a kinetic energy profile together the condition expressed in (1), at the inflow section, derived by the limiting values assumed by the velocity fluctuations at the end of the viscous sublayer in a fully-developed turbulent boundary layer [7]:

$$\begin{array}{l} w' \circ 0.5u' \\ v' \circ 0.75u' \end{array} \quad (5)$$

where u' is known by the experiments. Globally, U-ZEN has given similar results between the two grids, under the same boundary conditions, showing a strong sensibility to the inflow conditions. In fact, a remarkable difference of the case with the assigned k -profile can be seen especially in the boundary layer. The pressure coefficient on the hump is well predicted in the expansion zone, but after the separation, the results are generally inaccurate with a strong dependency on the turbulent model.

The FLUENT simulations have been carried out using the same grid used before (GRID1) with and without the cavity. The boundary conditions used are similar to what explained before, the only difference regards the treatment of turbulent quantities. For the SA model a constant turbulent viscosity ratio (equal to 10) is specified, whereas for the four equation model the same values used for the $k-\kappa$ model have been employed. The results are generally similar to the ones obtained with U-ZEN in the expansion zone, with a slight overprediction of the pressure peak at the leading edge of the bump (this was found to be extremely sensitive to the inlet and the upper wall boundary conditions). The separation zone is strongly influenced by the turbulence model, but both appear to underpredict the pressure level measured in the experiments. In particular, the ν^2-f model predicts a

lower level of the pressure but a better overall recovery in the reattachment region downstream of the bump.

Steady suction case.

For these simulations only the $k\text{-}\omega$ turbulence model has been used in U-ZEN and the SA model in FLUENT. The suction condition has been applied at the slot exit. The mass flow rate is constant along every section of the slot, while the momentum coefficient depends explicitly on the velocity magnitude. The simplest formulation used is to consider a top-hat velocity distribution applied along the d/c segment (see figure 1). The momentum coefficient will be scaled as follows:

$$C_\sigma/d^2 \propto C_\sigma/h^2 \propto \frac{h^2}{d^2} \quad (6)$$

where the superscript $()^+$ refers to the dimensionless quantities. Considering the figure 1, it is clear that the jet does not exit along the wall normal, but is inclined with a certain angle depending on the lateral wall inclinations and on the interaction with the external flow. Therefore, the problem of definition of a tangential velocity component arises. The second formulation consists in introducing a realistic direction by adding a tangential component that contributes to the C_σ and not to the mass flow. Assuming a vector notation, the effect of the jet angle can be considered as follows :

$$\frac{U_J^2}{k} \propto \frac{U_{Jn}^2}{2} + \frac{U_{Jt}^2}{2} \sqrt{k} \frac{d}{h} \tan^2 \chi \quad (7)$$

$$\begin{aligned} C_m &\propto \psi^2 U_{Jn}^2 h^2 \\ C_\sigma &\propto 2 \psi^2 U_{Jn}^2 / (2 k h^2) \end{aligned} \quad (8)$$

where χ is the angle between the wall normal and the jet direction, \underline{U}_{Jn}^2 and \underline{U}_{Jt}^2 are respectively the normal and the tangential components of \underline{U}_J^2 . Indeed, to take into account the stagnation region at the beginning of the orifice, (see figure 2), a value of d^+ less than the geometrical one can be considered. In this simulation the following values have been used:

$$\begin{aligned} \chi &= 43.9^\circ \\ d^+ &= 3.5 \cdot 10^{-3} \end{aligned}$$

In the figure 4, 5 and 6, the u-field component of the simulations with the whole cavity (FLUENT) , the wall normal jet, and the inclined one (U-ZEN) , can be seen. An improvement of the results has been obtained with the inclined model, although more accurate models could be defined. In fact, the treatment of the turbulent variables at the slot exit, here considered as a solid wall, is an open matter that could affect the solution quality.

Conclusions

From the analysis of the configuration without control, a strong sensitivity of the solution to the inflow and outflow conditions has been found. It's worth to note that the upper surface has been considered as a solid wall with a slip boundary condition, and it is not possible to exclude an influence of the upper boundary layer especially in the separated region (blockage effect, [8]) . In the

suction case, the computations simulating the whole cavity (FLUENT) and those applying the boundary condition at the slot exit (U-ZEN) are in a good agreement with the experimental data especially if the effect of the jet direction is taken into account. This is accomplished by adding a tangential component; the formulation of this boundary still does not include any modification of the turbulent variables. This would be the scope of future investigations.

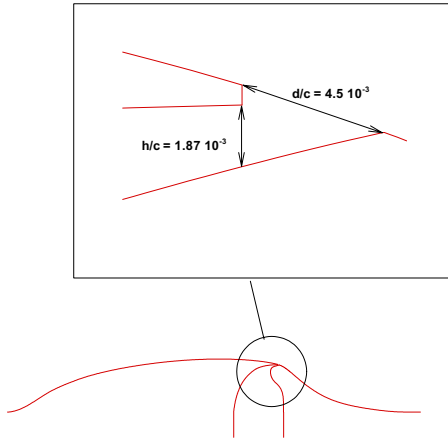


Figure 1- Slot exit detail

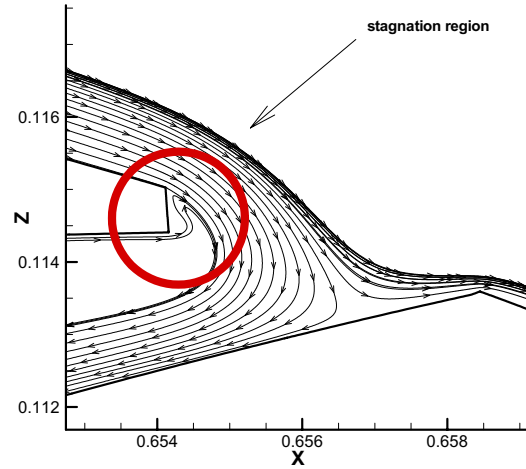


Figure 2 Cavity simulation. (Fluent) Detail on the stagnation region.

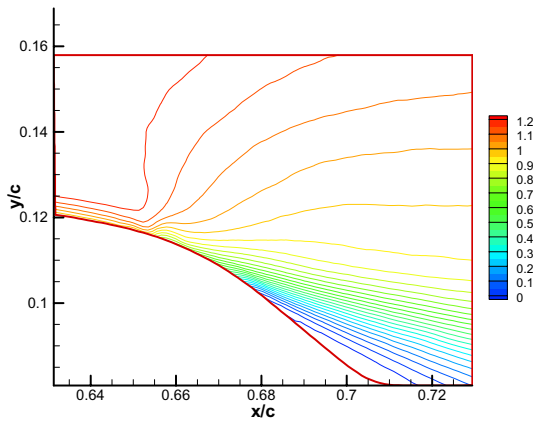


Figure 3 u-contours. Suction case. Experimental data

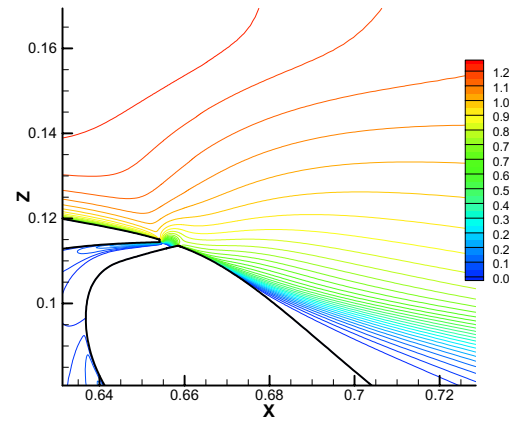


Figure 4 u-contours. Suction case. Cavity simulation (FLUENT)

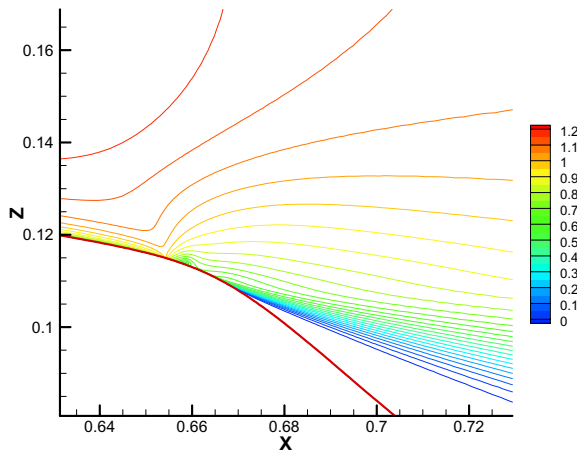


Figure 5 u-contours. Suction case. Wall normal jet.
(U-ZEN)

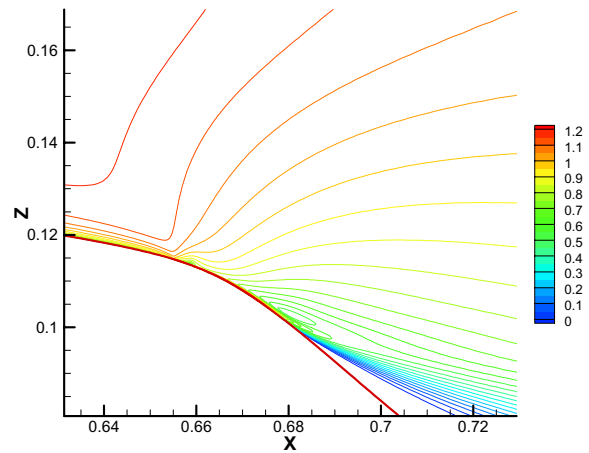


Figure 6 u-contours. Suction case. Inclined jet.
(U-ZEN)

References

- [1] Catalano, P., Amato, M., "An evaluation of RANS turbulence modeling for aerodynamics applications", Aerospace Science and Technology, Vol.7, No.7, October 2003, pg 493-590
- [2] Myong, H., Kasagi, N., "A new approach to the improvement of the k - κ turbulence model for wall bounded shear flows", JSME Intern. J. Ser.2 33 (1) 63-72.
- [3] Menter, F., R., "Two equation eddy viscosity turbulence models for engineering applications", AIAA J. 32 (8) (1994) 1598-1605.
- [4] Spalart, P. R., Allmaras, S., "A one-equation turbulence model for aerodynamic flows", AIAA 92-0439 (1992).
- [5] Durbin, P. A., "Separated Flow Computations with the k - κ - ν^2 model", AIAA J. 33 (1995) 659-664.
- [6] Iaccarino, G., "Prediction of a Turbulent Separated Flow Using commercial CFD Codes". J. Fluids Eng., V. 123, (2001) 815-824.
- [7] Mathieu, J., Scott, J., "An introduction to turbulent flow", Cambridge University Press 2000
- [8] Iaccarino, G., Marongiu, C., Catalano, P., Amato, M., "RANS simulation of the separated flow over a bump with active control", Annual Research Briefs 2003, Center for Turbulence Research, Stanford University/NASA Ames.

CASE 3: SYNTHETIC JET

3D STEADY HALF-DOMAIN COMPUTATION USING CFD++

S. Shariff, P. Batten

Metacomp Technologies, 28632-B Roadside Drive, Suite 255, Agoura Hills, CA 91301

Introduction

This paper briefly explains the details of one of our approaches to Case 3 of the Langley Research Center Workshop on synthetic jets. Here we have performed a three-dimensional simulation of half of the domain. For the suction case, we have prescribed the outflow pressure in the synthetic jet slot. This pressure was then adjusted to produce the appropriate mass flow through the slot.

Solution Methodology

This work was performed using CFD++, a Navier-Stokes solver for compressible and incompressible flow. CFD++ features a second order Total Variation Diminishing (TVD) discretization based on a multi-dimensional interpolation framework, which is also utilized for the viscous terms. A pre-conditioned HLLC (Harten-Lax-van Leer with Contact wave) Riemann solver is used to provide proper signal propagation physics while preserving positivity and satisfying the entropy condition. Further details regarding the numerical methodology can be found in Chakravarthy et al [2], Perroomian et al [4, 5], and Batten et al [1].

The simulations were computed with Metacomp's 2-equation cubic κ - ϵ RANS turbulence model, which is discussed in Palaniswamy et al [3].

Implementation and Case Specific Details

The grid was generated from the supplied geometry, and consists of 2.47 million hexahedral cells. The portion of the grid near the airfoil is shown in Figure 1 to give an idea of the stretching used. The grid was tightly stretched towards the bottom of the tunnel to directly resolve the boundary layer on the airfoil, but less tightly stretched at other walls. The domain extent in the streamwise direction was $-2.14 < x/c < 4.94$. The shorter domain was chosen because CFD++ allows the user to impose a fully-developed Musker boundary layer profile as a boundary condition, and the upper-wall boundary layer thickness was specified at $x/c = -2.14$. The lower boundary layer thickness for the Musker profile was estimated using the splitter plate length.

The outflow condition was set to a characteristics-based inflow/outflow condition. The equations were solved to the wall at the airfoil surface and lower tunnel wall, and wall functions were used for all other walls.

The flow in the slot was modeled, and for the suction case, a pressure-based inflow/outflow boundary condition was used at the bottom of the slot. This BC imposes the pressure in the case of outflow, and determines the state from the interior velocity in the case of inflow. Initially, the pressure was set to an arbitrary value somewhat less than the cavity pressure which developed in the no-suction case. This pressure was then adjusted to achieve the specified mass flux of 0.01518 kg/s through the slot (which corresponds to 0.00759 kg/s through the half-slot simulated here). This mass flux was ultimately achieved by setting the boundary pressure to 2100 Pa lower than the freestream, or 99.225 kPa.

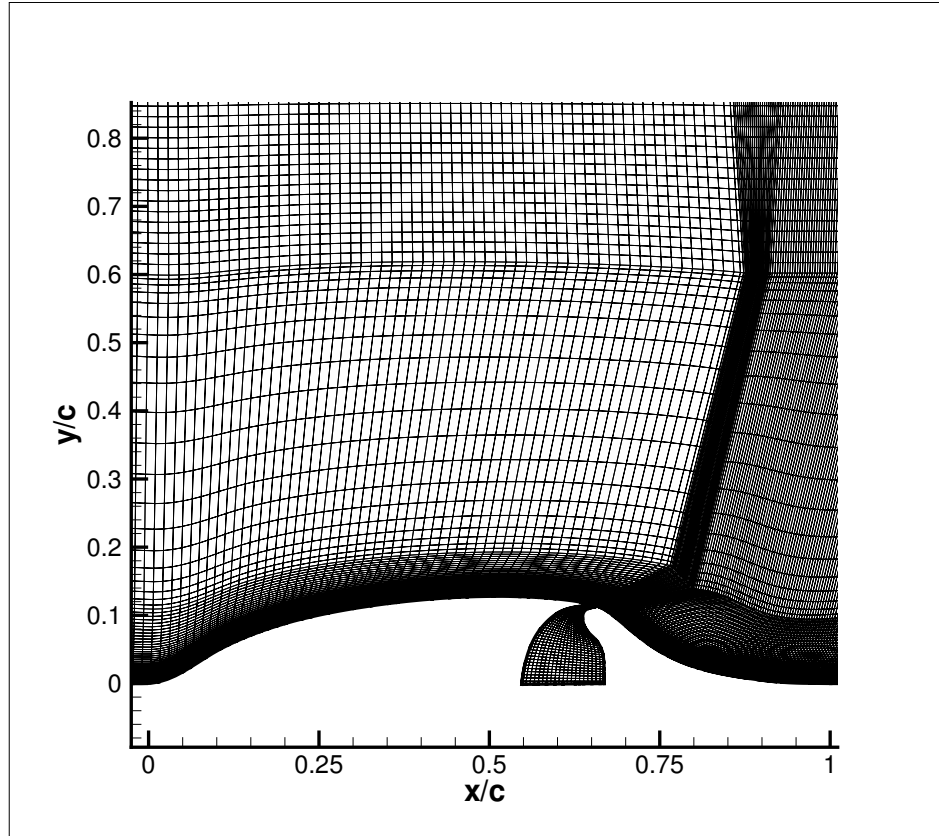


Figure 1: Grid detail near airfoil.

References

- [1] Batten, P., Leschziner, M.A. and Goldberg, U. "Average-state Jacobians and implicit methods for compressible viscous and turbulent flows," *J. Comp. Phys.*, Vol. 137, pp. 38-78.
- [2] Chakravarthy, S., Peroomian, O. and Sekar, B. "Some internal flow applications of a unified-grid CFD methodology," *AIAA Paper 96-2926*.
- [3] Palaniswamy, S., Goldberg, U., Peroomian, O. and Chakravarthy, S. "Predictions of Axial and Transverse Injection into Supersonic Flow," *Flow, Turbulence, and Combustion*, Vol. 66, pp. 37-55.
- [4] Peroomian, O., Chakravarthy, S. and Goldberg, U. "A grid-transparent methodology for CFD," *AIAA Paper 97-07245*.
- [5] Peroomian, O., Chakravarthy, S., Palaniswamy, S. and Goldberg, U. "Convergence acceleration for unified-grid formulation using preconditioned implicit relaxation," *AIAA Paper 98-0116*.

CASE 3: COMPUTATIONS OF FLOW OVER THE HUMP MODEL USING HIGHER ORDER METHOD WITH TURBULENCE MODELING

P.Balakumar

Flow Physics and Control Branch, NASA Langley Research Center, Hampton, VA 23681

Introduction

The flow over the two-dimensional hump model is computed by solving the RANS equations with k- ω (SST) model.

Solution Methodology

The governing equations, the flow equations and the turbulent equations, are solved using the 5th order accurate weighted essentially non-oscillatory (WENO) scheme for space discretization and using explicit third order total-variation-diminishing (TVD) Runge-Kutta scheme for time integration. The WENO and the TVD methods and the formulas are explained in [1] and the application of ENO method to N-S equations is given in [2]. The solution method implemented in this computation is described in detail in [3].

Model used

Standard k- ω (SST) model is used and the equations and the model coefficients are described in [4, 5, 6].

Implementation and Details

The computational domain extends from $x/c=-10$. to 4. in the streamwise direction and extends from the splitter plate to the upper tunnel wall in the normal direction. The leading edge of the splitter plate is modeled as a super ellipse with 0.25 in. half thickness and an aspect ratio of 2. The leading edge is located at $x/c=-5.9$. C-Type grid is used around the splitter plate and a rectangular grid is added upstream of the leading edge as shown in Fig. 1. This grid overlaps the C grid and 5th order central interpolation is used to transfer the flow variables from one grid to the other at the boundaries. (651*151) grid size is used around the splitter plate and the hump and (101*51) grid size is used in the rectangular region.

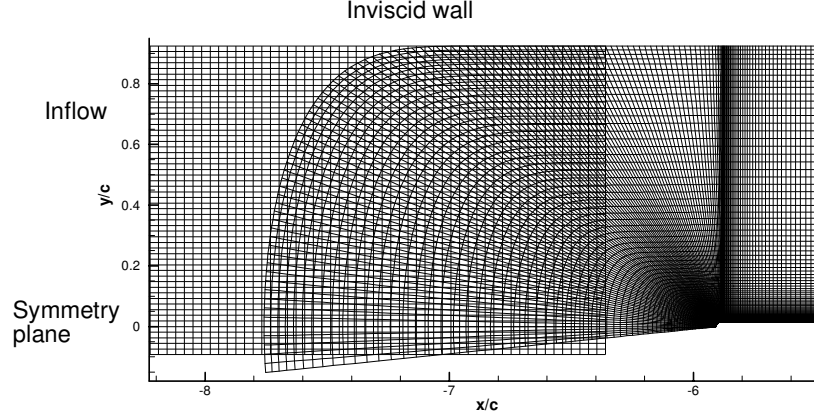


Figure 1: Overlapping grid near the leading edge of the splitter plate.

Following boundary conditions are implemented at different boundaries:

1. At the upper wall inviscid conditions are applied.

$$\frac{\partial \rho}{\partial y} = \frac{\partial u}{\partial y} = \frac{\partial E}{\partial y} = v = 0. \quad (1)$$

2. At the lower wall viscous conditions are used.

$$u = v = 0, \quad T = T_w = T_{free\ stream}, \quad (2)$$

and ρ is computed from the continuity equations.

3. From the leading edge of the splitter plate to the inflow boundary symmetric conditions are used.
4. At the inflow boundary stagnation pressure, one Riemann variable and normal velocity $v=0$ are prescribed and the second Riemann variable is solved for to obtain the other flow quantity.
5. At the outflow boundary the pressure is specified to obtain the required Mach number and characteristic-type boundary conditions are implemented similar to as described in [7] to obtain other flow variables.
6. In the suction case, boundary conditions are applied on the surface of the hump across the suction slot. The suction slot extends from $x/c=.6541$ to $.6584$ and across the slot normal mass flow rate is specified to the experimental value. A suction distribution of the form

$$(\rho v)_n = f_{\max} \sin^2 \frac{\pi(x - x_{start})}{(x_{end} - x_{start})} \quad (3)$$

is used. Other forms have been tried and all of them yield the same results for a fixed total suction rate. The other flow quantities are obtained using the characteristic type boundary conditions [7].

Following boundary conditions are implemented for the turbulent quantities at different boundaries.

1. At the inflow boundary small values are prescribed for k and μ_T .

$$\frac{k}{U_\infty^2} = 10^{-7}, \quad (4)$$

$$\frac{\mu_T}{\mu_\infty} = .009.$$

2. At the outflow boundary k and ω are solved for from the governing equations. Higher order extrapolation condition is also tried and it gives the same results.
3. At the lower viscous wall $k=0$ condition is used and following exact boundary condition is derived for ω .
4. In the suction case, across the suction slot linear extrapolation is used to obtain the turbulent quantities on the surface.

Since the variable ω becomes singular near a viscous wall, in practice a large approximate value is prescribed at the wall.

$$\omega_{wall} = \frac{60\mu_w}{\rho_w \beta d_w^2}, \quad (5)$$

where d_w is the distance to the first grid point from the wall. This is an approximate boundary condition and when it is implemented in the higher order scheme, oscillations and convergence problems are encountered and the following exact condition is derived for ω_{wall} . By realizing

that $\left\{ \frac{1}{y^2} \right\}$ type singularity for the variable ω arises because of the balance between the dissipation term and the viscous diffusion term in the ω equation, the singularity is removed by rewriting the variable ω as

$$\omega = \frac{C}{y_n^2} \omega_1, \quad (6)$$

where y_n is the normal distance to the wall, C is a constant and ω_1 is the new variable which is now regular near the wall. When this is substituted into the ω equation the following equation is obtained for ω_1 , which is similar to the ω equation except for the source term.

$$\begin{aligned} \frac{\partial}{\partial t}(\rho \omega_1) + \frac{\partial}{\partial x_j}(\rho u_j \omega_1) = & \rho \Omega^2 y_n^2 \text{Re} + \frac{1}{\text{Re}} \frac{\partial}{\partial x_j} \left\{ \left(\frac{\mu}{\sigma_w} + \frac{\mu_T}{\sigma_w} \right) \frac{\partial \omega_1}{\partial x_j} \right\} \\ & - \frac{\omega_1}{\text{Re}} \frac{1}{y_n^2} \left\{ \beta \rho \omega_1 - 6 \left(\frac{\mu}{\sigma_w} + \frac{\mu_T}{\sigma_w} \right) \frac{\partial y_n}{\partial x_j} \right\} \\ & - \frac{2}{y_n \text{Re}} \left\{ \left(\frac{\mu}{\sigma_w} + \frac{\mu_T}{\sigma_w} \right) \frac{\partial \omega_1}{\partial x_j} \frac{\partial y_n}{\partial x_j} + \frac{\partial}{\partial x_j} \left[\left(\frac{\mu}{\sigma_w} + \frac{\mu_T}{\sigma_w} \right) \omega_1 \frac{\partial y_n}{\partial x_j} \right] \right\} \\ & + \frac{2}{y_n} u_j \rho \omega_1 \frac{\partial y_n}{\partial x_j} + 2(1-F_1) \sigma_{\omega 2} \frac{\rho}{\omega_1} \frac{\partial k}{\partial x_j} \text{Re} y_n \frac{\partial \omega_1}{\partial x_j} y_n - 2 \frac{\partial y_n}{\partial x_j} \omega_1 \left\{ \right. \end{aligned} \quad (7)$$

The value of ω_1 at the wall becomes

$$\omega_{1wall} = \frac{6\mu}{\beta\rho} \left. \frac{\partial y_n}{\partial x_j} \right|_p. \quad (8)$$

Here the variable ω is nondimensionalised by

$$\omega = \frac{\omega^*}{\left. \frac{U_0^2}{\nu_0} \right|_C} \text{ and } C = \frac{1}{Re^2}. \quad (9)$$

Hence the procedure is to use the ω_1 equation for the first few points near the wall and switch to the ω equation away from the wall. In these computations ω_1 equation is solved for the first ten points near the wall. Figure 2 shows the distribution of k , ω and ω_1 near the wall and it is seen that this technique resolves the viscous layer smoothly even though ω is infinite at the wall.

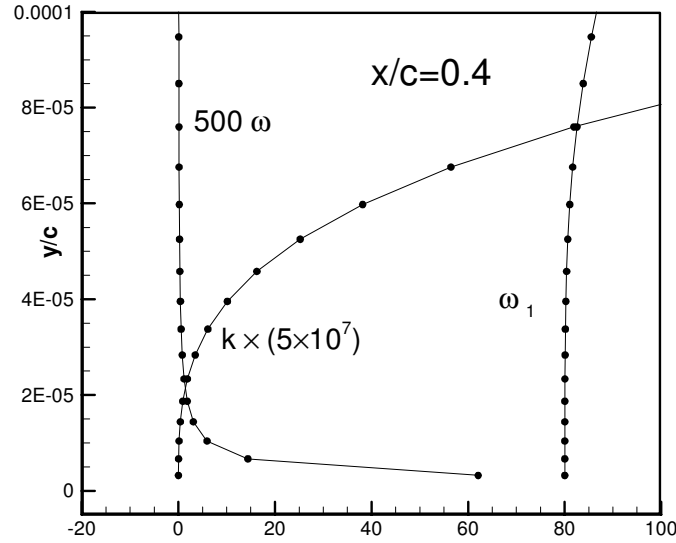


Figure 2: Variation of k , ω and ω_1 near the wall at $x/c=0.4$.

Figure 3 shows the contours of the U velocity near the leading edge region and for the entire computational domain. Near the leading edge region the flow separates and forms a small separation bubble. In the no flow case, the solution converged for the flow equations and the turbulent equations very well. In the suction case, the maximum residual in the ω equation near the suction slot edges converged only by three orders. This may be due to the boundary conditions used for the turbulent quantities near the suction slot.

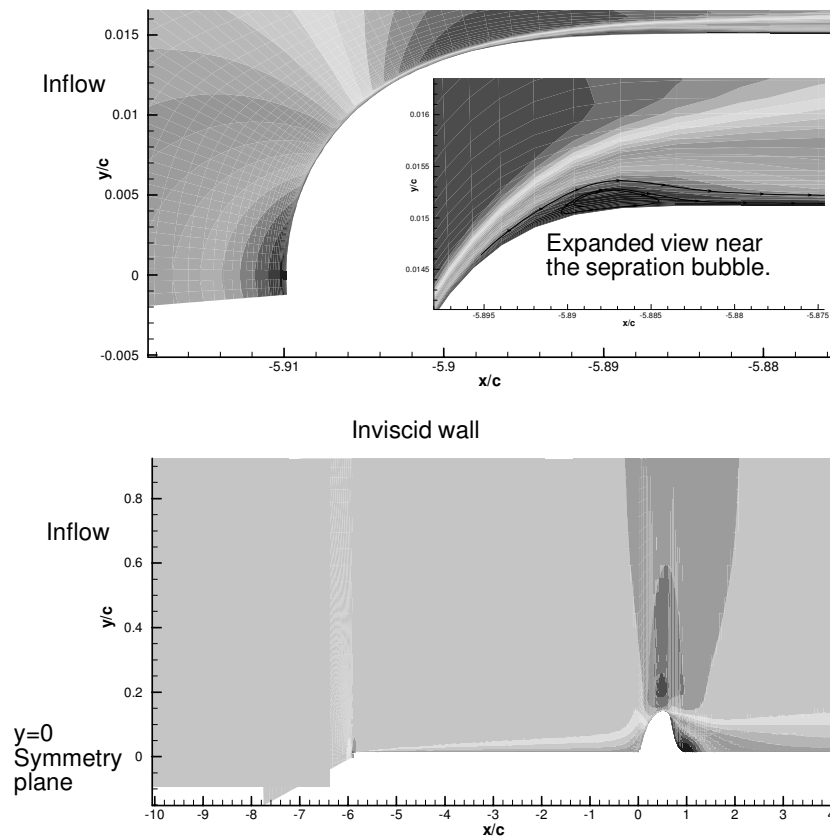


Figure 3: Contours of U velocity near the leading edge and over the hump.

References

1. Shu, Chi-Wang, "Essentially Non-Oscillatory and Weighted Essentially Non-Oscillatory Schemes for Hyperbolic Conservation Laws," *NASA/CR-97-206253 and ICASE Report* N0. 97-65, 1997.
2. Atkins, H. L., "High-Order ENO Methods for the Unsteady Compressible Navier-Stokes Equations," *AIAA Paper 91-1557*, 1991.
3. Balakumar, P., "Stability of Hypersonic Boundary-Layers Over a Compression Corner," *AIAA Paper 2002-2848*, 2002.
4. Menter, F. R., "Improved two-Equation $k-\omega$ Turbulence Models for Aerodynamic Flows," *NASA Technical Memorandum*, N0. 103975, 1992.
5. Menter, F. R., "Zonal Two Equation $k-\omega$ Turbulence Models for Aerodynamic Flows," *AIAA Paper 93-2906*, 1993.
6. Menter, F. R. and Rumsey, C. L., "Assessment of Two-equation Turbulence Models for transonic Flows," *AIAA Paper 94-2343*, 1994.
7. Sesterhenn, J., "A characteristic-type formulation of the Navier-Stokes equations for high order upwind schemes," *Computers & Fluids*, 30, pp. 37-67, 2001.

